

A neural network approach to event-by-event cosmic ray primary mass identification

S. Riggi*, R. Caruso, A. Insolia, M. Scuderi

Department of Physics and Astronomy, University of Catania, Italy

INFN, Section of Catania, Italy

*E-mail: simone.riggi@ct.infn.it, rossella.caruso@ct.infn.it,
antonio.insolia@ct.infn.it, mario.scuderi@ct.infn.it*

An event-by-event study, based on neural network method, of the mass identification in high energy cosmic rays was carried out with simulated data. Extensive air showers were simulated with the CONEX code, using the hadronic model QGSJET-II-3. The goodness of the method in recognizing the mass of the primary was tested making use of the parameters extracted from the simulated longitudinal profiles. We showed that the designed supervised neural network is able to discriminate, with high identification efficiency and purity, between proton- and iron-induced showers. We tested our method also in presence of a five components primary flux (proton, helium, oxygen, silicon and iron nuclei). A step further was moved by estimating the effect of the response of the fluorescence detector at the Pierre Auger Observatory over proton-iron identification. Typical results for the classification matrix obtained are presented and discussed.

*XI International Workshop on Advanced Computing and Analysis Techniques in Physics Research
Amsterdam, Holland
April, 23-27 2007*

*Speaker.

1. Introduction

Mass composition analysis is a fundamental task to test any theoretical model concerning the origin and the nature of the primary cosmic ray radiation at the highest energies. Different energy spectra are predicted to be observed at ground by the present theories, according to the mass of the primary particle, so the knowledge of the energy spectra for every mass component, or at least for groups of components, is required in order to discriminate among the proposed models.

At lower energies ($E < 10^{14}$ eV) the composition of cosmic rays can be measured using direct detection techniques, such as spectrometers and calorimeters.

At higher energies, the measurement of the mass is generally performed by indirect techniques, which make use of parameters sensitive to the primary mass, and determined by the shower development in the atmosphere. Among such parameters, X_{max} (the depth at which the longitudinal shower has its maximum), N_{max} (the number of shower particles at X_{max}) and N_{μ} (the number of muons at a given distance from the shower axis) are widely used. In the knee region ($10^{15} \div 10^{17}$ eV) a recent analysis from KASCADE experiment, based on the deconvolution of a 5-component mass spectra starting from the experimental N_e - N_{μ} scatter plots, shows that the knee is due to a decrease of the light component with respect to the heavier one, and that the knee position for higher masses shifts towards higher energy [1]. A clear increase of the mean logarithmic mass as a function of the primary energy is found in other experiments, such as EASTOP-MACRO [2]. While the experimental results show a definite trend in this intermediate energy region, the situation becomes controversial moving to the highest energies ($> 10^{17}$ eV): the HiRes analysis [3], based on the elongation rate method, the Yakutsk analysis [4], based on the comparison of experimental X_{max} distributions to QGSJET simulated ones, and the AGASA analysis [5], based on the comparison of experimental muon number distributions with simulated ones, suggest a composition dominated by the proton component. Recent re-analyzed data from Volcano Ranch [6] and Haverah Park [7] experiments, based on the comparison of the steepness parameter distributions, extracted from the lateral distribution function, with simulated ones, claim for a composition dominated by the iron component.

Interesting attempts to compare these results are found in [8] and [9]. Measurements from different experiments are difficult to compare, because the predictions are strongly dependent upon the hadronic models used in the analysis. These controversial results suggest that the problem of mass composition at the highest energies is still open and debated.

Two kinds of approaches can be used to perform a composition analysis: the event-by-event approach uses pattern recognition methods, working with a set of shower parameters sensitive to the mass, in order to estimate the probability of identifying the mass of every observed event; methods of unfolding or deconvolution allow to infer the energy spectra for different mass components, starting from a data set of shower parameters, without any care regarding the mass of the single event.

It is clear that a mass identification study must be necessarily restricted to limited mass groups, since the absence of features strongly correlated with the primary mass and the presence of stochastic shower-to-shower fluctuations in the shower parameters, make a complete analysis very inefficient. The first approach could become inadequate, even with a powerful pattern recognition method, especially with a too large number of mass components. Keeping in mind these difficul-

ties, an event-by-event reconstruction is anyway necessary if one wants to study possible correlations with other analysis, e.g. if one wants to correlate the mass of an event with its astrophysical arrival direction.

For these reasons we present in this paper the results of an event-by-event study using a neural network as identification tool and discriminating parameters which could be measured by an air-fluorescence telescope such as in the Pierre Auger Observatory or the Hi-Resolution Fly's Eye. A similar approach has been discussed by A.K.O. Tiba et al. [11] and by M. Ambrosio et al. [12].

The paper is organized as follows: section II gives a brief introduction of the Pierre Auger Observatory, section III describes the data set, built from CONEX simulations of extensive air showers, and the parameters sensitive to the mass, used as network inputs. Section IV presents the designed neural network and its application to simulated data. Section V, finally, shows the obtained results and our conclusions.

2. The Pierre Auger Observatory

The Pierre Auger Observatory has been designed to study the ultra-high energy cosmic rays (UHECR) in the GZK cutoff region with an unprecedented statistics and precision.

The observatory will consist of two sites, one in each hemisphere. The Southern Observatory, currently under construction close to the city of Malargue in Argentina, is expected to be completed at the end of this year and is taking data as the deployment goes on. The Northern site will be

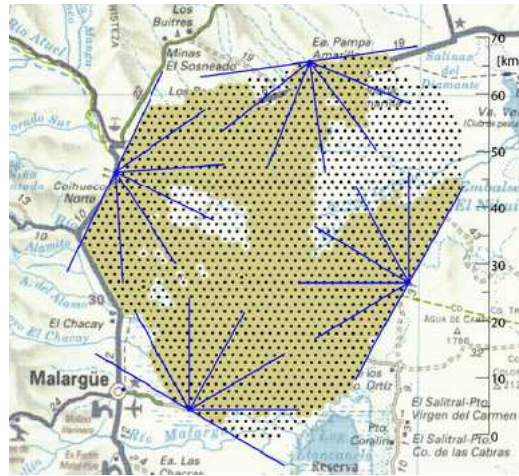


Figure 1: The Southern Observatory in May 2007, showing the positions of the four FD stations and the approximately 1200 deployed SD tanks (shaded region).

located in Southeast Colorado and is actually in project phase.

The Southern Observatory is made up of two systems of detectors: a surface detector (SD), which is a grid of 1600 equally spaced Cherenkov water tanks, extending over an area of 3000 km^2 , with 1500 m spacing between detectors. Each tank contains 12 tonnes of water (10 m^2 area), and each is equipped with three $9'$ PMTs, local digitizing electronics (400 MHz sampling rate), solar power, GPS receiver and a radio communication system.

The fluorescence detector (FD) is made up of 4 fluorescence eyes, equipped with 6 telescope each,

located at the array vertex. Each telescope is built with a Schmidt optics allowing the elimination of the coma aberration: a circular diaphragm of radius 1.10 m is located at the center of curvature of the spherical mirror. An UV transmitting filter placed in the entrance aperture reduces the background light and provides protection from outside dust. A series of Schmidt corrector elements are located just inside the UV filter. The light is focused by a large 3.5×3.5 m spherical mirror, with curvature radius of 3.4 m, onto a spherical camera, which hosts an array of 440 hexagonal pixels of 1.5° diameter. Pixel signals are digitized with 100 MHz sampling.

Figure 1 shows the actual status of the deployment: the array will be completed at the end of the year, while the FD has been completed, as soon as the Loma Amarilla eye has started operation in February 2007.

The SD observes the shower front, by measuring the particle density at ground level: this detector can operate all the time with a duty cycle of 100%. The FD measures the fluorescence light emitted by the shower particles traversing the atmosphere: the duty cycle in this case is reduced to about 10%, since the telescopes can operate only in the clear moonless nights.

The unique hybrid combination of fluorescence and surface detectors has enormous advantages in all objectives of the Observatory. For example, in the study of the ultra-high energy cosmic ray energy spectrum the SD provides the energy parameter $S(1000)$, a huge collecting area, 24 hr operation and an easily calculable aperture. The FD provides the conversion between $S(1000)$ and the cosmic ray primary energy, since the FD uses a near-calorimetric technique for determining energy. This avoids calibrating $S(1000)$ via shower simulations, which have uncertainties related to hadronic interaction models.

In anisotropy studies, hybrid data provide high-precision shower arrival directions which are used to cross-check SD-derived directions and to directly measure the SD angular resolution.

In mass composition studies, the FD measures the longitudinal shower profile, which could be used, as we would like to show, as promising mass sensitive observable, in combination with SD parameters.

3. The simulated data

This study is based on a sample of simulated showers, which were generated with CONEX 1.4 [13] [14], using QGSJET II-03 as hadronic interaction model.

At the present state, CONEX allow only a one-dimensional simulation of the cascade, with smaller CPU times with respect to the ones needed by typical three-dimensional code, such as CORSIKA or AIRES. This feature makes CONEX very suitable for FD applications, in particular, for the analysis of the shower longitudinal profiles.

The simulated data set is made of:

- 36000 protons
- 34000 helium nuclei
- 29000 oxygen nuclei
- 32000 silicon nuclei

- 29000 iron nuclei

with uniform energy and zenith angle distributions in the range $10^{18} - 10^{19}$ eV and $0^\circ - 60^\circ$, respectively. We made use of the amount of information contained in the simulated longitudinal curves, sampled in 10 g/cm^2 bins by CONEX, with the profiles limited to the range $200\text{-}870 \text{ g/cm}^2$. These limits approximate the best viewing conditions of existing FD devices such as in the Auger Observatory or the HiRes.

In order to perform a composition study, we need a set of parameters sensitive to the primary mass: the discrimination among the different components is done using the well known fact that heavy primary induced showers develop faster in the atmosphere with respect to light induced ones (e.g. they reach the cascade maximum at smaller atmospheric depths), because of the higher nucleus-air cross section for showers of the same primary energy and zenith angles.

We extracted the following set of parameters from the longitudinal curves to show this behavior:

- X_{max} , N_{max} : atmospheric depth of shower maximum and number of charged particles at shower maximum;
- $p10$, $p50$, $p90$: atmospheric depths at which the 10%, 50%, 90% of the whole integral profile are reached. These are sort of indicators about the “rise-and-fall time” of the longitudinal profiles;
- E , θ : primary energy and zenith angle (these are not directly correlated with the mass).

The numerical values of the first two parameters (X_{max} and N_{max}) were evaluated by fitting the simulated profiles $N_{ch}(X)$ for charged particles in the range $200\text{-}870 \text{ g/cm}^2$ with a standard 6-parameters Gaisser-Hillas function:

$$N_{ch}(X) = N_{max} \frac{X - X_0}{X_{max} - X_0} \frac{X_{max} - X_0}{a + bX + cX^2} \exp\left(\frac{X_{max} - X}{a + bX + cX^2}\right) \quad (3.1)$$

The integral I of the whole profile in the above-mentioned range was evaluated by numerically integrating the profile curves, specified at a certain number of points (at least greater than 4), with a NAG routine, which evaluates the integral using a third-order finite-difference formula, according to a method due to Gill and Miller [15]. The integral between successive points is calculated by a four-points finite-difference formula centered on each interval, except in the case of the first and last intervals, where four-points forward and backward difference formulae respectively are employed.

The values of the parameters $p10$, $p50$, $p90$ were then determined interpolating with a first-order polynomial in the interval, inside of which the required $10\%I$, $50\%I$, $90\%I$ integrals are reached. The choice of using such NAG routine is motivated by the fact that it does work with unequally-spaced points, as the points of the experimental profiles actually are.

The parameter space built in this way is therefore suitable for the neural network method application.

4. Neural network application to simulated data

This section presents the application of a neural network technique to the identification problem, describing the design of the network used, and the steps followed to perform the analysis.

4.1 The network design

A feed forward neural network (NN) is structured in parallel layers of neurons, connected to neurons in adjacent layers by weighted connections, indicating the strength of the neuron link. The input layer is connected to the input data vector and an indefinite number of hidden layers process the signal towards the output layer which returns the final response of the network to the presented input data. The basic processing unit in the network is the neuron: the input signals x_i ($i=1,m$)

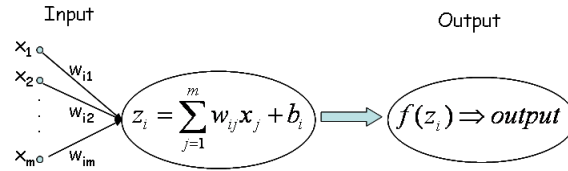


Figure 2: A single neuron of index i : the input vector components x_i , the weights w_{ij} ($j=1,\dots,m$), the biases b_i , the transfer function f and the output signal $f(z_i)$ are showed.

coming from each input channel are linearly transformed by applying a multiplicative weight w_{ij} and an additive bias b_i to form the net neuron input z_i :

$$z_i = \sum_{j=1}^m w_{ij} x_j + b_i \quad (4.1)$$

The neuron output is obtained by applying a transfer function $f(z_i)$ to the net input (see Figure 2). Common forms of such activation functions are the simple linear function $f(z_i) = \alpha z_i + \beta$, or the sigmoidal form functions, as well as the logistic function $f(z_i) = \frac{1}{1 + \exp(-\alpha z_i)}$ and the hyperbolic tangent function $f(z_i) = \frac{\exp(z_i) - \exp(-z_i)}{\exp(z_i) + \exp(-z_i)}$.

After testing several network architectures, we obtained good results using a net with an input vector of dimension 7, 3 hidden layers, each one with 10 neurons, and an output layer with one neuron. The activation functions are hyperbolic tangent in the hidden layers and linear in the output layer.

Next step is the choice of the training algorithm. The training data is a set of N events (\mathbf{x}_i, y_i) $i = 1, \dots, N$, defined by the 7-dim input vector $\mathbf{x}_i \equiv (X_{max}, N_{max}, E, \theta, p10, p50, p90)_i$ and by the desired output vector (the mass identity of the event) y_i . The supervised training algorithm minimizes the difference between the desired output y_i and the network computed output t_i , by adjusting iteratively the weights and biases of the net in order to minimize a given error function E . The error function used for the present analysis is the standard square error function:

$$E = \frac{1}{2} \sum_{i=1}^N [y_i(\mathbf{x}, \mathbf{w}) - t_i]^2 \quad (4.2)$$

Some backpropagation training algorithms have been tested (steepest descent, conjugated gradient and quasi-Newton algorithms). We achieved better identification performances with quasi-Newton methods, since other algorithms often return bad or local minima of the error function. We used a quasi-Newton algorithm with the Broyden-Fletcher-Goldfarb-Shanno (BFGS) error minimization formula [16][17].

Next subsection will describe the identification procedure we followed.

4.2 The identification method

The identification analysis proceeds as follows:

- *Pattern selection*: we divided the simulated shower set in three independent subsets (learn, validation and test data set), the first used to train the network, the second to stop the training phase and check the net generalization capabilities and the last to evaluate the achieved performances.
- *Feature pre-processing*: we normalized the features in the range $[-1,1]$ to avoid large dynamics among the network inputs;
- *Training phase*: we trained the network to return a value of 0 or 1 in presence of a proton or iron event, respectively. The learning phase was stopped at a given epoch when the network began to show a clear overtraining behavior, corresponding to a loss of generality in the identification procedure, e.g. when the network error calculated over the test sample stopped to fall down and began to increase.
- *Evaluation of the results*: we evaluated the performances of the method by means of the identification efficiency ϵ and purity P for a given mass class i of primaries :

$$\epsilon^{(i)} = \frac{N_{right}^{(i)}}{N_{true}^{(i)}} \quad (4.3)$$

$$P^{(i)} = \frac{N_{right}^{(i)}}{N_{right}^{(i)} + \sum_{j \neq i} N_{wrong}^{(j)}} \quad (4.4)$$

where N_{true} , N_{right} and N_{wrong} represent the true number of events for the given mass class, the number of correctly identified events and the number of misclassified events. N_{right} was evaluated through a cut over the network output: events with an output smaller than 0.5 were recognized as protons, otherwise as iron nuclei.

5. Results

In this section we report the results of the classification analysis, in terms of the achieved identification efficiency and purity.

5.1 Results with pure simulated data

Figure 3 shows the outputs computed by the net in presence of the test set. The dashed blue histogram corresponds to the true proton events, while the red one, located above 1, represents the true iron events. As we can clearly see, the net is able to associate the proton and iron events to the desired outputs with very little misclassifications.

The identification efficiency and purity, relative to the chosen cut at 0.5, are shown in Table 1 for the proton and iron mass classes.

We tested our method also in presence of a five components primary flux (proton, helium, oxygen,

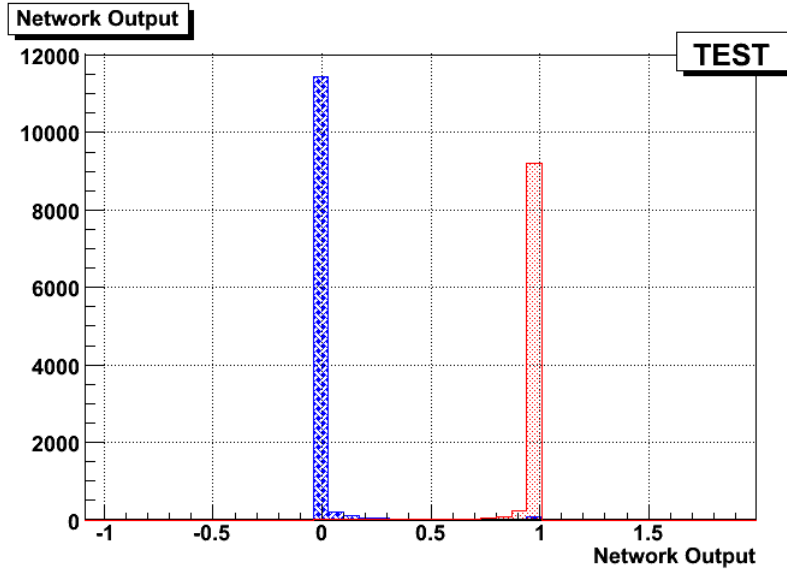


Figure 3: Output computed by the net in presence of the test set. The dashed blue histogram (left) corresponds to the true proton events, while the red histogram (right), located above 1, represents the true iron events.

Table 1: Identification efficiency, eq. (4), and purity, eq. (5), for the training, validation and test samples.

	LEARN		VALIDATION		TEST	
	$\varepsilon(\%)$	$P(\%)$	$\varepsilon(\%)$	$P(\%)$	$\varepsilon(\%)$	$P(\%)$
p	98.96	99.65	98.77	99.60	98.81	99.51
Fe	99.57	98.72	99.51	98.49	99.40	98.54

silicon and iron nuclei) assigning a desired net output of 0, 1, 2, 3, 4 respectively, to the five classes. Results are showed in Figure 4. By cutting at 0.5, 1.5, 2.5 and 3.5 we separated the five classes, obtaining the classification matrix showed in Table 2.

Table 2: Classification matrix and identification purity for the training, validation and test samples.

	LEARN					Purity
	Classification $P_{C_i \rightarrow C_j}(\%)$					
	$C_j = p$	$C_j = He$	$C_j = O$	$C_j = Si$	$C_j = Fe$	
$C_i = p$	68.37	29.14	2.27	0.21	$8.32 \cdot 10^{-3}$	72.77
$C_i = He$	26.93	60.52	11.21	1.31	0.04	55.89
$C_i = O$	0.14	18.76	56.33	23.47	1.29	56.43
$C_i = Si$	0.06	0.90	24.59	64.00	10.45	60.57
$C_i = Fe$	0.00	0.04	0.37	20.74	78.84	85.95

The diagonal values are the identification efficiency of the four classes, while the non-diagonal elements give information about the misclassification of a class with respect to the others. Results

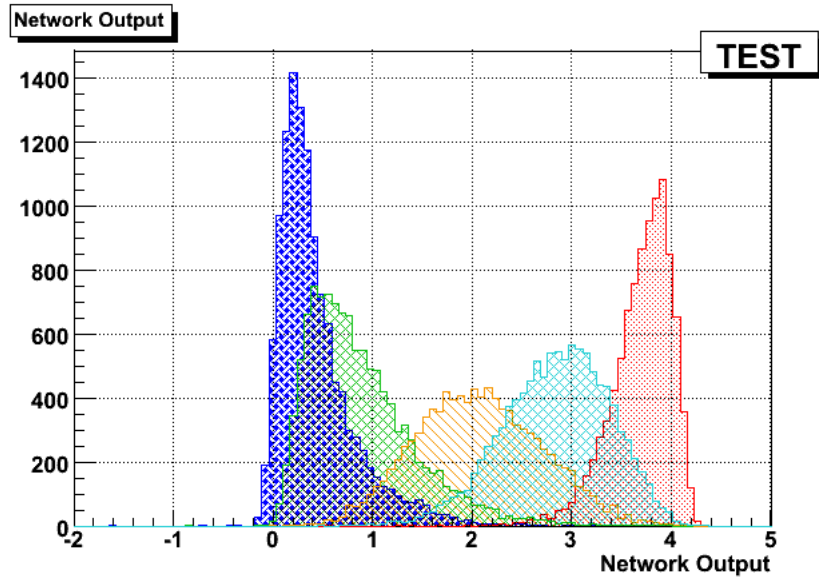


Figure 4: Output computed by the net in presence of the test set. The first (left) and the last (right) histograms correspond to the true proton and iron events, while the three lower histograms correspond to the true helium, oxygen and silicon events, respectively from left to right.

VALIDATION						
	Classification $P_{C_i \rightarrow C_j}$ (%)					Purity
	$C_j = p$	$C_j = He$	$C_j = O$	$C_j = Si$	$C_j = Fe$	
$C_i = p$	69.05	28.49	2.28	0.18	$8.38 \cdot 10^{-3}$	73.24
$C_i = He$	26.48	60.81	11.70	0.93	0.07	56.13
$C_i = O$	0.22	19.21	55.52	23.86	1.19	55.29
$C_i = Si$	0.02	1.05	25.46	62.90	10.57	59.82
$C_i = Fe$	0.00	0.02	0.33	21.32	78.32	85.85

TEST						
	Classification $P_{C_i \rightarrow C_j}$ (%)					Purity
	$C_j = p$	$C_j = He$	$C_j = O$	$C_j = Si$	$C_j = Fe$	
$C_i = p$	69.36	28.13	2.35	0.15	0.00	73.07
$C_i = He$	26.83	60.57	11.20	1.30	0.10	56.52
$C_i = O$	0.22	18.62	56.39	23.61	1.17	56.61
$C_i = Si$	$9.32 \cdot 10^{-3}$	1.00	24.28	64.36	10.36	60.25
$C_i = Fe$	0.00	0.05	0.31	21.63	78.01	85.97

show that the lightest and heavier components are better reconstructed, while a stronger contamination is found in the intermediate components.

5.2 Taking into account the FD response

Final step of the present analysis is the evaluation of the identification efficiency including the response of the fluorescence detector alone. We decided to restrict the analysis to the proton and iron components.

CONEX showers were simulated in the field of view of LosLeones detector at the Pierre Auger Observatory, by randomly choosing the core positions, as showed in figure 5.

Simulation and reconstruction phase were performed using the official *Offline* framework at the

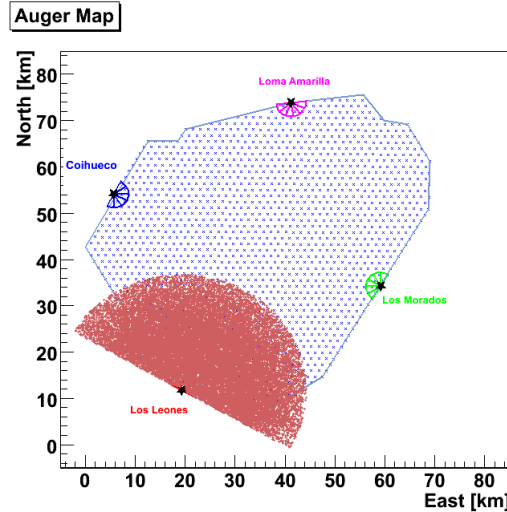


Figure 5: Core positions of the simulated events in the Auger map: red dots represent the event cores, generated inside a semicircle of radius 20 km around LosLeones detector. The positions of the Cherenkov tanks and the other three fluorescence detectors are also showed, even if these detector are not used in the simulation and reconstruction step.

Auger Observatory.

Simulation phase involves the simulation of the shower at some distance from one of the eyes, generation of the fluorescence and Cherenkov light emitted by the shower as it develops and propagation of the emitted photons to the telescope aperture. Final step include the simulation of the PMTs response and triggering, up to the second trigger level (SLT).

The reconstruction phase was carried out, beginning with calibration of the fluorescence telescopes, a procedure which transforms simulated raw data into physical quantities. A standard value of 5 was used as conversion factor photons/ADC counts. Afterwards a pulse finding algorithm is used to further process the traces recorded by the fluorescence telescopes. Next, a series of geometrical reconstruction modules are employed. First the plane containing the shower axis and the eye which detected it is determined. A geometrical fit within this plane is performed, taking into account the timing of the shower image as it traverses the telescope pixels. A calculation of the light flux reaching the telescope aperture is then carried out. The last step is the profile reconstruction, which converts the fluorescence light profile recorded by the telescopes to a determination of the energy deposit at a given atmospheric depth along the shower axis.

The events fed into the neural network were subjected to a series of quality cuts: the main cuts applied require a good fit of the longitudinal profile with a reduced chi square less than 5.

During the training phase we encountered an early loss of the network generalization capabilities: we faced this problem by adding a regularization term to the mean square error function of the net to avoid larger value weights, as showed below:

$$REGMSE = \gamma MSE + (1 - \gamma) \sum_{i=1}^{N_w} w_i^2 \quad (5.1)$$

with $\gamma = 0.5$ and N_w equal to the number of weights in the network.

In figure 6 we show the response of the network in presence of the reconstructed events.

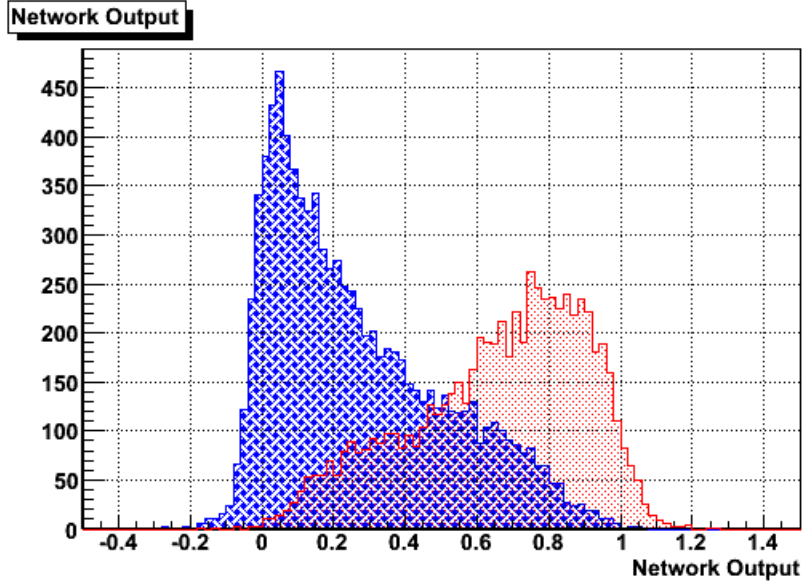


Figure 6: Output computed by the net in presence of a test set, made up of reconstructed events. The dashed blue histogram (left), located above 1, corresponds to the true proton events, while the red histogram (right) represents the true iron events.

Table 3: Identification efficiency, eq. (4), and purity, eq. (5), for the train and test samples.

	LEARN		TEST	
	$\epsilon(\%)$	$P(\%)$	$\epsilon(\%)$	$P(\%)$
p	81.60	80.52	80.70	80.72
Fe	74.14	75.47	74.70	74.68

Results obtained for the classification efficiency and purity are showed in Table 3: as we expected, the performance drops below of around 20% with respect to the pure simulated events. We point out that this results are to be regarded as a first estimate of the performance of the method, since many factors have to be still taken into account, first of all the atmospheric conditions, in order to report conclusive values for the classification matrix. As soon as the matrix elements are well known, together with their uncertainties, they can be freezed, and it will be possible to deconvolute the effects of the misclassification and get the reconstructed number of events of each mass in a data sample.

6. Conclusion and future perspectives

We proposed and tested the neural network approach to the mass identification problem of high energy cosmic rays.

We studied mass discrimination in the case of CONEX simulated showers with a 2-components (proton and iron nuclei) and 5-components (proton and helium, oxygen, silicon and iron nuclei) mass flux, making use of parameters from the longitudinal profiles. In the first case we obtain excellent performances, with very small misidentification probabilities, of the order of 2%.

In the second case we found misclassification probabilities of 30%, 40%, 44%, 36% and 22% for the considered mass classes. The identification performances varied very little even if we tried to slightly modify the network architecture, e.g. varying the number of hidden layers and the number of neurons per layer.

We evaluated the performance of the method taking into account the response of the FD in the case of proton and iron events: the obtained identification efficiency drops down at the level of 80% and 75% respectively.

A more accurate work is planned: the effects of different atmospheric conditions over mass identification should be taken into account, we would like to restrict the analysis to smaller energy bins and release a final classification matrix for each bin.

Possible future developments could be the increase of the number of mass components and the number of network inputs, by including also observables measured with the SD.

Acknowledgments

The authors thank Prof. M. Russo for remarks and useful discussions.

References

- [1] T. Antoni et al, *KASCADE measurements of energy spectra for elemental groups of cosmic rays: Results and open problems*, *Astropart. Phys.* **24** (1) 2005.
- [2] G. Navarra, *Spectrum and mass composition of the high energy galactic radiation*, *Nucl. Phys. B (Proc. Suppl)* **136** (265) 2004.
- [3] G. Thomson, *New Results from the HiRes Experiment*, *Nucl. Phys. B (Proc. Suppl)* **136** (28) 2004.
- [4] S.P. Knurenko et al, *Characteristics of EAS and primary particle mass composition in the energy region of 10^{17} - $3 \cdot 10^{19}$ eV by Yakutsk data*, *Nucl. Phys. B (Proc. Suppl)* **151** (92) 2006.
- [5] K. Shinozaki, *AGASA results*, *Nucl. Phys. B (Proc. Suppl)* **151** (3) 2006.
- [6] M.T. Dova et al, *The mass composition of cosmic rays near 10^{18} eV as deduced from measurements made at Volcano Ranch*, *Astropart. Phys.* **21** (597) 2004.
- [7] M. Ave et al, *Mass composition of cosmic rays in the range 2×10^{17} – 3×10^{18} eV measured with the Haverah Park array*, *Astropart. Phys.* **19** (61) 2003.
- [8] A.A. Watson, *The mass composition of cosmic rays above 10^{17} eV*, *Nucl. Phys. B (Proc. Suppl)* **151** (83) 2006.

- [9] B.R. Dawson et al., *A Comparison of Cosmic Ray Composition Measurements at the Highest Energies*, *Astropart. Phys.* **9** (331) 1998.
- [10] P. Mantsch, *The Pierre Auger Observatory progress and first results*, [astro-ph/0604114].
- [11] A.K.O. Tiba, G.A. Medina-Tanco, S.J. Sciutto, [astro-ph0502255].
- [12] M.Ambrosio et al, *Comparison between methods for the determination of the primary cosmic ray mass composition from the longitudinal profile of atmospheric cascades*, *Astropart. Phys.* **24** (355) 2005.
- [13] T. Pierog et al, *First results of fast one-dimensional hybrid simulation of EAS using CONEX*, in proceedings of 13th International Symposium on Very High-Energy Cosmic Ray Interactions, *Nucl. Phys. B (Proc. Suppl.)* **151** (159) 2006, [astro-ph/0411260]
- [14] N.N. Kalmykov et al, *One-dimensional hybrid approach to extensive air shower simulation*, *Astropart. Phys.* **26** (420) 2007.
- [15] P.E. Gill and G.F. Miller, *An Algorithm for the Integration of Unequally Spaced Data*, *Comput. J.* **15** (80) 1972.
- [16] C.M. Bishop, *Neural Networks for Pattern Recognition*, Oxford University Press 1995.
- [17] H. Demuth and M. Beale, *Neural Network Toolbox, MATLAB User's Guide version 5*, 2006.